Induced-seismicity geomechanics for controlled CO_2 storage in the North Sea (IGCCS)

Joonsang Park [a,*], Luke Griffiths [a], Jérémie Dautriat [b], Lars Grande [a], Ismael Vera Rodriguez [c], Kamran Iranpour [c], Tore I. Bjørnarå [a], Héctor Marín Moreno [a,d], Nazmul Haque Mondol [a,e], Guillaume Sauvin [a], Joel Sarout [b], Magnus Soldal [a], Volker Oye [c], David N. Dewhurst [b], Jung Chan Choi [a], Angus Ian Best [d]

[a] NGI - Norwegian Geotechnical Institute, Oslo 0806, Norway
[b] CSIRO Energy, Kensington, WA 6151, Australia
[c] NORSAR, Kjeller 2007, Norway
[d] National Oceanography Centre, European Way, Southampton SO14 3ZH, United Kingdom
[e] Department of Geosciences, University of Oslo, Oslo 0371, Norway

ABSTRACT

The aim of the current study, IGCCS (2017–2020), is to evaluate the feasibility of micro-seismic (MS) monitoring of CO_2 injection into representative storage candidates in the North Sea, based on broad and quantitative characterization of relevant subsurface behavior with respect to geology, geomechanics and seismicity. For this purpose, we first group potential CO_2 storage sites in the North Sea into three different depths. Then, advanced triaxial rock mechanical tests are performed together with acoustic emission (AE) acquisition under representative loading for CO_2 storage sites in the North Sea and for formations of each depth group, covering shale, mudstone and sandstone cores. Our work focuses particularly on quantifying the effects of injected fluid type and temperature on mechanical behavior and associated MS response of subsurface sediments. The experiment results show that each depth group may behave differently in responses to CO_2 injection. Particularly, the occurrence of detectable MS events is expected to increase with depth, as the combined effects of rock stiffness and temperature contrast between the host rock and injected CO_2 are increasing. In addition, lithology plays an important role in terms of the MS response, i.e. high AE event rate is observed in sandstones, while aseismicity in shale and mudstone. The test results are then scaled up and applied to advanced coupled flow-geomechanics simulations and a synthetic field-scale MS data study to understand micro-seismicity at fracture, reservoir and regional scales. The numerical simulation of $scCO_2$ injection scenario shows quite different stress-strain changes compared to brine injection, resulting mainly from the thermally-induced behavior. Furthermore, the numerical simulation study via so-called Cohesion Zone Modeling (CZM) approach shows strong potential to improve our understanding of the multiphase-flow-driven fracture propagation. Our synthetic MS data study, focused on slow-earthquake scenario, also suggests that sensors with high sensitivity at low frequency might be necessary for better signal detection and characterization during CO_2 injection. This manuscript covers the main findings and insights obtained during the whole study of IGCCS, and refers to relevant publications for more details.

1. Introduction

Carbon-dioxide Capture and Storage (CCS) involves: efficient capture of CO_2 at large-scale sources (e.g., fossil-fuel power plants, waste-to-energy plants, heavy industries such as steel, cement); safe transport to qualified geological storage sites; permanent storage of CO_2 in the subsurface; cost-effective monitoring of the storage complex; and verification that the whole CCS value-chain behaves as expected. All these stages must be fulfilled at high technology readiness level so that CCS can be fully accepted by all stakeholders as a green-house gas control solution in order finally to meet the targeted maximum of 2 °C temperature increase before the end of this century. Many developed and

developing countries are currently joining forces to improve CCS technologies in the different stages mentioned above. Norway is at the forefront of this effort and plans to operate the first full-chain offshore CCS project (*Longship*) in the North Sea in few years. The transportation and storage components of *Longship* are operated by the Northern Lights project as a partnership between Equinor, Shell and TotalEnergies. As mentioned above, the CCS technology involves many different stages and stakeholders. Therefore, CCS is an intensive and challenging task. Fortunately, the oil and gas industry's long-term experience provides useful and key competences to allow CCS to be realized in a timely fashion. Many innovative research and development activities are ongoing globally and it is also expected that CCS will create significant economic opportunities worldwide.

To ensure safe offshore CO_2 storage operations and to minimize the risk of CO_2 leakage to seabed (i.e. storage conformance and containment), geophysical characterization and monitoring are essential, which is commonly performed using 4D streamer seismic rather than ocean bottom seismic (OBS) for CO_2 storage. At the same time, passive microseismic (MS) monitoring shows strong potential among the available geophysical approaches thanks to its continuous acquisition (e.g. via OBS) and no requirement for any active marine seismic source. Furthermore, induced-seismicity is related directly to local *in-situ* stress state and changes in pore pressure and thus effective stress during injection operations. Nevertheless, MS monitoring of CO_2 storage has not yet been performed in the North Sea. Before MS can be reliably and efficiently used as a monitoring technique, there are knowledge gaps that need to be addressed, including technical improvements in offshore seismometer networks (Oye et al., 2021), and quantitative understanding of the effects of pore pressure, fluid type, and temperature change on geomechanics and micro-seismicity. MS monitoring is based on the continuous measurement of seismic signals triggered by relatively abrupt subsurface movements such as the formation and/or re-activation of faults and fractures. Interpretation of MS data in terms of geomechanical behavior (i.e. stress and strain) requires quantitative understanding of couplings between geology, geomechanics and seismicity. The current study (IGCCS) aims to address this fundamental knowledge gap and to evaluate the feasibility of MS monitoring for CO_2 injection into storage candidates in the North Sea. We also demonstrate how to utilize MS data to ensure that CO_2 injection operations are geomechanically-safe and that any hazardous damage to the reservoir and overburden is prevented in upcoming CO_2 storage projects in the North Sea.

In IGCCS, advanced rock mechanical laboratory tests are performed in combination with numerical simulations at field scale. The laboratory work includes acoustic emission (AE: laboratory-scale microseismicity) acquisition to analyze MS sources under controlled stress conditions, representing real injection scenarios. Through this advanced laboratory test program, we have also developed material models for large-scale geomechanical modeling of North Sea CO_2 storage candidates. The learnings from our laboratory testing are then scaled up through a synthetic data study to apply to field-scale scenarios. The field-scale study aims to provide insights into (1) expected geomechanical behaviour of the North Sea storage sites during CO_2 injection, and (2) planning of cost-effective MS surveys, data processing and interpretation. The rock samples tested for the laboratory experiment are a set of North Sea shale, mudstone, and sandstone cores from various formations and depths (including the Draupne and Sognefjord Formations), as well as analogue sandstones such as Grès des Vosges and Red Wildmoor. The core plugs are tested under confining stress and pore pressure conditions representative of the North Sea. Our focus is particularly on the following fundamental mechanisms: (1) differences in geomechanical response between CO_2 and brine injections; and (2) thermal effects due to cold CO_2 injection. The current paper provides a brief summary of the main findings and learnings from IGCCS, and for more details, refers to the IGCCS-related publications of Bjørnarå et al. (2021a, 2021b), CLI-MIT, 2020, Fawad and Mondol (2019), Grande et al. (2020), Griffiths et al. (2019, 2021), Mondol et al. (2018) and Mondol (2019).

The current manuscript is structured as follows. Section 2 presents representative geological and geomechanical models in the North Sea, which cover shallow, intermediate and deep reservoir storage potential in the North Sea. In addition, a brief overview of all the laboratory tests performed in IGCCS is provided. Section 3 then summarizes the key learnings from the laboratory tests with particular focus on (1) the influence of fluid type on fracturing and AE response of a deep reservoir sandstone analogue; and (2) geomechanical material models (covering sandstone, mudstone, and shale). Section 4. describes all the main insights learned from the advanced numerical simulation study and discusses them together with our laboratory observations and existing published literature. Section 5 addresses how all the learnings achieved through laboratory tests and numerical simulations can be applied at the field scale with focus on a particular type of event, so-called slow event. Finally, Section 6 provides summary and conclusion.

2. Representative geomodels and tested cores for North Sea CO_2 storage sites

First, we describe the representative geological and geomechanical models for CO_2 storage candidates in the North Sea, which is based on a literature review (including existing laboratory data, well logs, etc.) and laboratory tests performed in the current study. The candidates are categorized into three different depths: shallow ($<$ 1000 m, e.g. Utsira, Skade), intermediate (1000–2000 m, e.g. Smeaheia), and deep ($>$ 2000 m, e.g. Aurora).

For the shallow-depth candidate, we select the Visund sandstone (about 1400 m deep) for reservoir and the Nordland mudstone (about 700 m deep) for sealing, which are taken from the southern Viking Graben and are the representative analogue core samples of a shallow storage candidate with a rather poorly consolidated loose sandstone overlaid by softer mudstone sealing unit. This shallow candidate is known as one of the largest aquifer systems in the North Sea (the Skade-Utsira aquifer) spanning over both the Norwegian and UK sectors and has been considered to have large-scale storage potential (Norwegian Petroleum Directorate, 2014). Several studies have also focused on the Sleipner storage project in the Utsira Formation where CO_2 has been injected since 1996 at a rate of approximately 1 Mt/year. Extensive monitoring data and research related to the Sleipner operation have contributed to improve our understanding of geological CO_2 storage (e.g Arts et al., 2008.; Zhu et al., 2015; Park et al., 2017). Furthermore, the Skade Formation below the Utsira Formation has also been evaluated for the assessment of CO_2 storage capacity and multiphysics-based monitoring (i.e Elenius et al., 2018.; Tveit et al., 2020).

For the intermediate-depth candidate, we select the Smeaheia storage complex, of which an extensive data package is available in the public domain (Gassnova, 2020). The Smeaheia area is approximately 20 km east of the Troll East field and situated in the Stord Basin of water depth about 320 m. The storage unit is structurally shallower than the Troll field (Fig. 1a). Two wells are available, i.e. Well 32/4-1 (Alpha structure, Smeaheia west) and Well 32/2-1 (Beta structure, Smeaheia east). The former penetrates 68 m of Sognefjord Formation sands, while the latter penetrates 114 m of Sognefjord Formation sands. In the current study, Well 32/4-1 (Alpha structure) is mainly utilized for petrophysical analysis and rock physics diagnostics to characterize the reservoir sandstones in the Smeaheia area (Mondol et al., 2018; Mondol, 2019). The reservoir sandstone is uncemented and has good-to-excellent reservoir quality. The reservoir can also be subdivided into three zones, of which the lower unit (Zone-3) has an excellent reservoir quality (high porosity, high permeability and lower clay content) compared to the two upper units (Zone-1 and Zone-2). Two carbonate stringers are also present in Zone-3 and interpreted as extremely high resistivity, high density, high acoustic velocity and low porosity/permeability units which could be flow baffles or even barriers, depending on their spatial distribution e.g. lateral extent. Well 32/4-1 also has a range of porosities
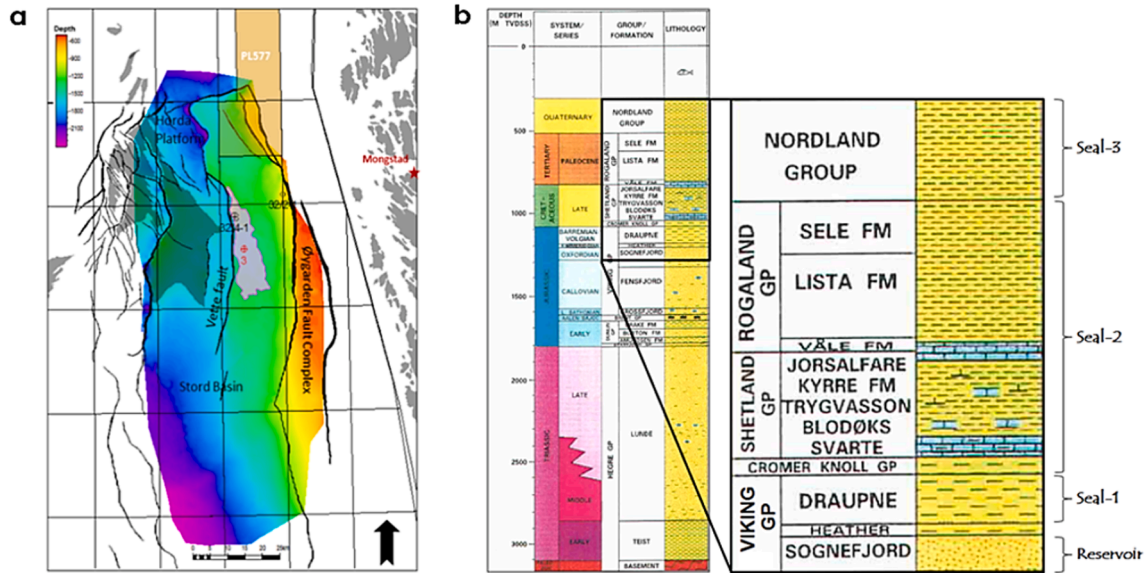
Fig. 1. (a) Top Sognefjord Formation depth and structural map (Well 32/4–1 and Well 32/2–1) with one of the 3 suggested drilling locations for CO_2 injection and plume migration after approximately 500 years (adapted from Gassnova 2020); (b) Stratigraphic column of Well 32/4–1 (Alpha Structure) showing the target CO_2 storage reservoir of the Sognefjord Formation and its primary, secondary and tertiary seals (Source: NPD FactPages). (Mondol et al., 2018).

(25–35%), with an average porosity of 30% (Mondol et al., 2018). The main cap rock covering the Sognefjord reservoir is the Upper Jurassic Draupne Formation which is a marine, organic rich, impermeable claystone (Fig. 1b). Secondary seal units are present in the form of Cretaceous limestone and shales belonging to the Shetland and Cromer Knoll groups. Furthermore, Tertiary and Quaternary deposits above are also expected to have extra sealing capacity. There is no Draupne core available from the Smeaheia and Troll areas for the current study.

Instead, we have performed laboratory tests with the Draupne samples from Well 16/8-3S drilled in the Ling depression in the Central North Sea (Skurtveit et al., 2015). Note that this core represents a deeper overburden sealing unit, e.g. more relevant to the deeper prospect like the Aurora CO_2 storage candidate, south of the Troll West field. No uplift has been suggested in the location of Well 16/8–3S (Hansen et al., 2017), while the Draupne formation in the Smeaheia and Troll areas has been significantly uplifted, i.e. 1100 m for Smeaheia and 800 m for Troll

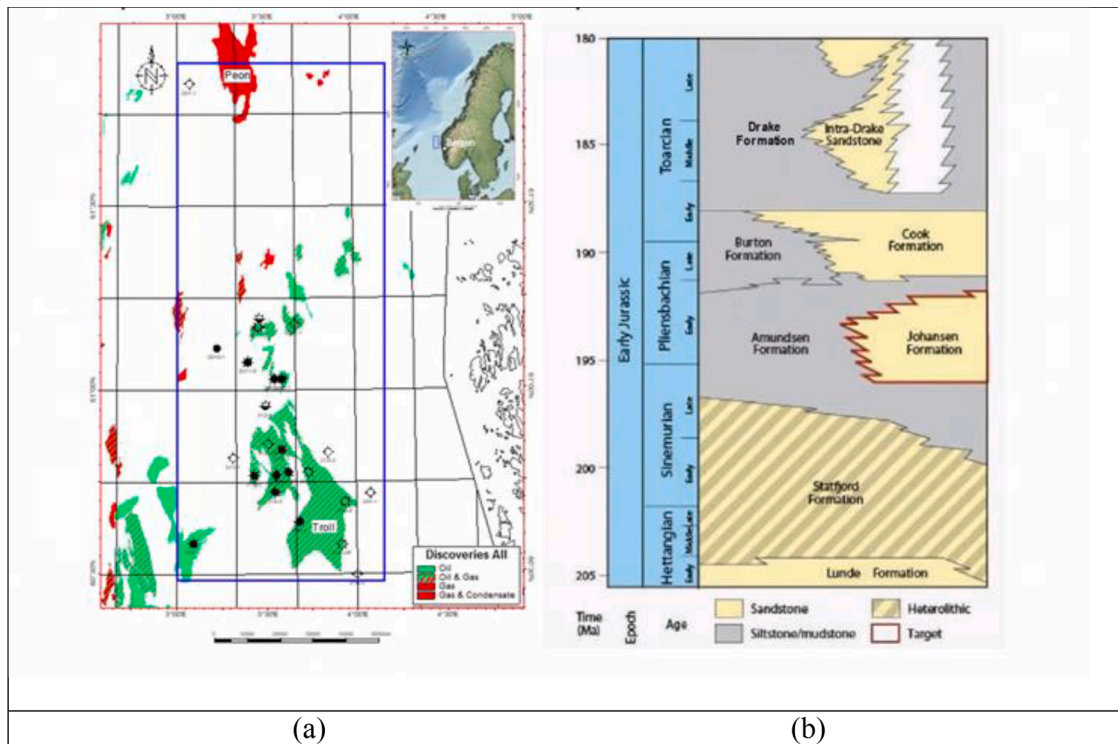

Fig. 2. (a) Map of the larger Troll area and the locations of wells studied for evaluation of sealing units of the Drake and Amundsen Formations lying within the blue rectangle (Fawad and Mondol, 2019). The Aurora field is south of Troll (not shown on this map). (b) Stratigraphic positions of the Amundsen, Drake and Johansen Formations within the area of study (Sundal et al., 2015, 2016).

East (Grande et al., 2020) and as such, the geomechanical behaviour may be distinctly different (i.e. over-consolidated vs. normally consolidated).

For the deep candidate in this study, we select the Aurora field, south of the Troll West field, a promising CO_2 storage alternative selected by the Northern Lights project, with a storage depth in the range of 2.5–3 km (Equinor, 2020). Regional studies of well logs in the larger Troll area indicate a depth range of around 1800–4200 m TVDSS for sealing units of the Drake and Amundsen Formations, and the depth range of 1660–4100 m TVDSS for the Johansen reservoir unit (Fawad and Mondol, 2019; Fig. 2a). These studies highlight large petrophysical variations in both the reservoir and sealing units with depth. Namely, the porosity in the Johansen Formation varies significantly (4–34%) with a depth-dependant trend, and there are also variations in quartz cement depending on clay content. The quartz/silica cementation is pervasive in the cleaner sandstones, whereas sandstones with shale volume (V_{sh}) of 30–40% are the least cemented. Chlorite is an important component in the North Sea sandstone reservoirs, and chlorite-coated quartz grains are common in the samples from the Johansen Formation (Sundal et al., 2015, 2016; Fig. 2b). Rock physics analyses of the Amundsen and Drake Formations confirm the increase in brittleness owing to the increase of quartz cementation, depth and temperature (Fawad and Mondol, 2019). The Upper Jurassic Draupne Formation (equivalent to the Kimmeridge Formation) is found throughout the Norwegian Continental Shelf (NCS) as main source, carrier or seal rock in several hydrocarbon fields. The Draupne Formation is an organic-rich shale deposited in a low-energy intra-shelf marine environment. In the North Sea, the Draupne Formation is penetrated by exploration wells at various depth levels (from 800 to 6000 m) and has been substantially indurated by burial and later uplifted where the maximum uplift has

occurred towards the coast (Mondol, 2019). However, no core is available from the Johansen, Drake and Amundsen Formations for the current study. Instead, a Draupne shale core from Ling Depression (2584 m) is tested and further studied together with the results from previous testing (Mondol, 2019), since it has similar burial depth to the Aurora storage candidate (2.5–3 km). However, it should also be noted that the organic-rich Draupne shale differs in composition and burial history in comparison to the sealing of the Aurora field.

The geomechanical properties are compiled from extensive laboratory test data, both pre-existing (Grande and Cuisiat, 2008) and newly acquired in IGCCS (Mondol et al., 2018; CLIMIT, 2020; Grande et al., 2020, CLIMIT, 2020; Griffiths et al., 2021); the laboratory data is upscaled through correlations with logs for the relevant North Sea lithologies (Horsrud, 2001). The compiled laboratory data includes those produced in IGCCS in order to obtain not only extended geomechanical properties of the North-Sea-specific materials at relevant stress levels and stress paths, but also AE responses and insights. Two multistage triaxial tests combined with AE acquisition are performed on intermediate-depth sandstone cores of the Sognefjord Formation (Troll field, Well 31/6-6, depth 1610 m) and shallow sandstone cores from the Visund area (depth 1418 m) (CLIMIT, 2020). The Troll sandstone is relevant for the Smeaheia area and the Visund sandstone is relevant to the shallow Utsira/Skade aquifers. In addition, multistage triaxial tests are performed on two caprock lithologies as well: one with shallow (700 m) mudstone from Nordland Group and the other with a deeply-buried (2581 m) shale from the Draupne Formation (CLIMIT, 2020; Grande et al., 2020). Furthermore, two reservoir sandstone analogues, Red Wildmoor and Grès des Vosges, are also tested (Griffiths et al., 2019, 2021), which can be relevant for the intermediate depth Sognefjorden (Smeaheia) and the deeper Johansen Formations (Aurora), respectively.

Table 1

Overview of IGCCS test plan. Data for all tests (mechanical, ultrasonic velocity, acoustic emissions (AE) is available in the supplementary data package). Note that stresses given in the table are the consolidation stresses prior to shearing.

Category	Field/Area	Lab	Test No.	Pore fluid	Vertical effective stress [MPa]	Effective horizontal stress [MPa]	Pore pressure [MPa]	Temperature [°C]	AE events detected
Sandstone	Red Wildmoor	NGI	T2308	Dry	0.3	0.3	–	Room temperature (RT)	Yes
Sandstone	Red Wildmoor	NGI	T2312	Dry	3	3	–	RT	Yes
Sandstone	Grès des Vosges	NGI	T2314	Brine (35 g/L)	11	11	1	RT	Yes
Reservoir	Troll	NGI	T2320	Oil (Marcol 52)	13.3	5.4	1	RT	Yes
Caprock	Draupne	NGI	T2333	Brine (35 g/L)	25.8	17	30	RT	No
Sandstone	Red Wildmoor	CSIRO	2856	Dry	3	3	–	RT	Yes
Sandstone	Grès des Vosges	CSIRO	2861	Brine (35 g/L)	11	11	1	RT	Yes
Sandstone	Grès des Vosges	CSIRO	2862	CO_2	31	18	9	65	Yes
Sandstone	Grès des Vosges	CSIRO	3036	Brine (35 g/L)	31	18	9	65	Yes
Sandstone	Grès des Vosges	CSIRO	3037	CO_2 + residual brine (35 g/L)	31	18	9	65	Yes
Reservoir	Troll	CSIRO	3041	CO_2 + residual brine (35 g/L)	13.3	5.4	9	60	Yes
Reservoir	Troll	CSIRO	3043	CO_2 + residual brine (35 g/L)	13.3	5.4	9	60	Yes
Reservoir	Visund	CSIRO	3044	CO_2 + residual brine	13.3	5.4	9	60	Yes
Caprock	Nordland	NGI	T2364	Brine (35 g/L)	7	4	8	RT	No
Caprock	Draupne	CSIRO	3099	Brine (35 g/L) + CO_2	25.8	17	9	60	No
Reservoir	Visund	CSIRO	3250	CO_2 + residual brine (35 g/L)	1	1	9	60	Yes
Reservoir	Visund	NGI	T2409	Brine (35 g/L) saturated	3	3	9	RT	Yes
Reservoir	Visund	NGI	T2411	Brine (35 g/L) saturated	1	1	9	RT	Yes
Reservoir	Visund	NGI	T2412	Brine (35 g/L) saturated	3	3	9	RT	Yes

Tables 1–3 summarize, respectively, all the tests performed in IGCCS, the geomechanical parameters extracted from the tests performed on the overburden and reservoir lithologies, and the compiled *in-situ* stresses for different lithologies and depths. The best estimate of *in-situ* stress profile for the Smeaheia storage (intermediate) is based on a depletion scenario (Gassnova, 2020), while the other CO_2 storage candidates are assumed to be in a normal pore pressure regime (hydrostatic). The reservoir *in-situ* effective vertical stress and the effective horizontal stress at the Smeaheia site are estimated at the injection point (1488 m TVD msl) and top reservoir (1304 m TVD msl), and the stresses and pore pressure for the Sognefjord Formation given in Table 3 are based on the assumption of 4 MPa initial depletion for the reservoir. In contrast, the initial stress and hydrostatic pore pressure is given for the cap rock above the Sognefjord Formation. For the shallow storage candidate, the *in-situ* stress in the Utsira/Skade formation at a depth of the top Utsira reservoir (855 m) is calculated based on the assumption of hydrostatic pore pressure as in Elenius et al. (2018). Unfortunately, the stress data of the Aurora storage site (deep candidate) were not available during the IGCCS project period. Hence, the stresses from the Draupne core test (CLIMIT, 2020; Grande et al., 2020) are applied for the evaluation of this deep storage candidate. Note that the Draupne core's depth (2.6 km) is within the same range as the Aurora depth (2, 3 km). However, note that the Aurora site in the Horda platform has undergone erosion and uplift during its burial history, potentially impacting the density, stresses and geomechanical behaviour of the overburden, which are not fully considered in the current study.

The parameters in Tables 2 and 3 are applied to the analytical evaluation for the poro-thermo-elastic response during uniaxial strain, based on Fjær et al. (2008), of the potential stress path and micro-seismicity likelihood during CO_2 injection (CLIMIT, 2020) Fig. 3. shows one example of the results of the simplest loading cases i.e. the stress paths induced by purely thermal (left column) and purely pore pressure (right column) loading changes, covering shallow, intermediate and deep reservoirs (from the top to bottom rows). More details and the other loading cases, including pressure-temperature-combined, can be found at CLIMIT, 2020. Here, we discuss only the main observations from the analytical evaluation of AE/MS likelihood of the North Sea lithologies, concerning thermal-influence zone, far-field area, and cap rock.

- Thermal-influence zone: Intensive events may develop due to increased shear stress during mean effective stress unloading (i.e. stress path moves towards a failure envelope), resulting from the simultaneous change of pore pressure increase and formation temperature cooling near injection wells. Namely, the stress path deviates from the uniaxial condition, resulting in increased vertical strain (i.e. compaction rather than expansion due to reduced radial stress during cooling). This observation is based on one of the Visund sample tests under effective stress unloading and constant shear stress (T2412 in Table 1).
- Far-field area: Limited number of events are expected, resulting from pore pressure increase and mean effective stress unloading, without significant thermal influence. This area likely represents a large part of the reservoir with the exception of reservoir boundaries, and areas close to faults or with complex geometries. This expectation is according to one of the Troll sample tests with axial and uniaxial unloading phases (T2320 in Table 1).
- Cap rock lithologies: No AE events are recorded for both shallow mudstone and deep shale from the AE laboratory testing (T2333, T2364, 3099 in Table 1), although sheared to failure at high shear stress level, compared to one expected in the cap rock during CO_2 injection. This highlights the potential of aseismicity or slow earthquake behavior in shale, which might be a challenging factor for MS monitoring.

Table 2

Geomechanical parameters extracted from tests performed in IGCCS (CLIMIT, 2020).

Lithology and depth	Young's modulus and velocities	Shear strength data of intact and fractured rock	Geological information of the lithologies tested
Visund sandstone 1418 m	$E_{initial} = 0.63$ GPa $E_{50} = 0.26$ GPa $\upsilon = 0.3$ $V_{pax} = 2020$ m/s $V_{prad} = 2200$ m/s	$C = 0.45$ MPa $\Phi = 19.1°$	No XRD data available from this depth; V_p and V_s at 3 MPa; No failure plane generated; therefore no data for C_{remob} and Φ_{remob}; $E_{initial}$ at 3 MPa and initial shear stress, and E_{50} at 2.5 MPa shear stress.
Sognefjord Sandstone 1610 m	$E_{load} = 2.02$ GPa $E_{unload} = 5.2$ GPa $\upsilon_{unload} = 0.18$	$\tau_{peak} = 24$ MPa $C_{remob} = 1$ MPa $\Phi_{remob} = 35.5°$	Porosity of 28% and a dry density of 1.8 g/cm³; Well 32/4–1 has a similar range of porosities (25–35%), with an average porosity of 30% (Mondol et al., 2018).
Nordland mudstone 700 m	$E_{unload} = 1.25$ GPa $E_{reload} = 1.1$ GPa $E_{initial} = 0.3$ GPa $E_{50} = 0.14$ GPa $V_{pax} = 2258$ m/s $V_{prad} = 2213$ m/s	$\tau_{peak} = 2.65$ MPa $C_{remob} = 0.8$ MPa $\Phi_{remob} = 20.4°$	Porosity of 39 - 41%; permeability of 1.6×10^{-3} mD; bulk mineralogy of 68% clay, 19% Quartz, 7% K-feldspar, 5.5% plagioclase, with a minor amount of Calcite and Pyrite (Mondol et al., 2010).
Draupne shale 2584 m	$E_{initial} = 5.6$ GPa $E_{50} = 2.5$ GPa* $V_{pax} = 2739$ m/s $V_{prad} = 3313$ m/s	$\tau_{peak} = 15.33$ MPa $C_{remob} = 1.45$ MPa $\Phi_{remob} = 19.2°$	Porosity of 6.5–12.5%; permeability of $1–6 \times 10^{-7}$ mD; bulk mineralogy of 48% clay 24% Quartz, 18% Feldspar 3% Pyrite and 2% Carbonates and (Skurtveit et al., 2015). *: Mondol (2019)

Symbols used: E_{unload}, E_{reload}, $E_{initial}$, and E_{50} are Young's modulus during unloading, E_{reload}, initial loading, and 50% of shear mobilization, respectively; C and Φ are the cohesion coefficient and friction angle, respectively, for intact rock; C_{remob} and Φ_{remob} are the cohesion coefficient and friction angle, respectively, for remobilization on induced fracture from test; τ_{peak} is the peak shear strength. Vpax and Vprad are axial and radial P-velocities.

3. Acoustic emission (AE) and mechanical testing of rock

As mentioned earlier, advanced mechanical testing campaigns are performed in the current study with the aim of generating an extensive and unique database of the geomechanical properties of reservoir and cap rocks, as well as for the evaluation of MS potential under stress-strain conditions relevant to CO_2 injection in the North Sea (shown in Table 1). The main test results are summarized briefly here with particular focus on: (1) the influence of pore fluid type on fracturing and AE response of a deep reservoir sandstone; and (2) geomechanical material models (covering sandstone, mudstone, and shale). More details, including the AE data processing workflow developed in IGCCS, are reported at CLIMIT, 2020, Grande et al. (2020), and Griffiths et al. (2019, 2021).

3.1. Influence of pore fluid on lab-scale microseismicity

Three triaxial tests are performed on the Grès des Vosges sandstone, which is an analogue rock to a deep North Sea reservoir sandstone, i.e. the Johansen Formation at the Aurora site. Three samples are saturated with either scCO₂, brine, or brine-scCO₂ mixture (i.e. first brine-saturated and then flushed with scCO₂) to investigate the influence of fluid type on mechanical properties, failure criteria and microseismic response. Each sample is sheared at confining stresses relevant to the

Table 3.
Summary of *in-situ* stresses for lithologies at representative (shallow, intermediate, and deep reservoirs), simplified from CLIMIT, 2020. These stresses are inputs to the analytical evaluation.

Relative depth	Reference lithologies	Reference depthm TVD	Effective vertical stress (MPa)	Effective horizontal stress(MPa)	Pore pressure (MPa)	Effective stress ratio (K_0)	Refs.
Shallow	Caprock Nordland	855 m	7.77	4.66	8.65	0.60	Depth 855 mTVD top Utsira reservoir; Stress based on assumptions for Utsira/Skade with shallow sealing units (Elenius et al., 2018); Horizontal stress gradient 13.4 MPa/km; Vertical stress from average density 2.1 g/cm^3
	Reservoir Utsira/Skade	855 m (top reservoir)	7.77	2.81	8.65	0.36	
Intermediate	Caprock Draupne	1304 m (top reservoir)	10.23	5.53	13.17	0.61	All data from Gassnova (2020); Values of stress and pore pressure for reservoir refers to 4 MPa depletion and adjustment of horizontal stress from using a Poisson's ratio of 0.18.
	Reservoir Sognefjorden	1488 m (injection point)	16.20	9.60	11.00	0.59	
Deep	Caprock Drake/ Amundsen	2584 m	25.8	17.0	25.9	0.66	No stress data available; Use stress from Draupne Ling depression (Skurtveit et al., 2015); Depth Aurora 2–3000 m; Assume lower K_0 in reservoir.
	Reservoir Cook/Johansen	2584 m	25.8	10.3	25.9	0.40	

North Sea to first induce a fracture, which is then reactivated. Fractures are reactivated first by increasing pore pressure, and then by axial reloading. The results are summarized in Table 4. The scCO$_2$-saturated sample is slightly stronger and stiffer than the two other samples. Introducing CO$_2$ into the brine saturated sample (i.e. brine-scCO$_2$ mixture) shows no significant changes on strength and stiffness. Both the pore-pressure reactivation stress and the loading reactivation stress are lowest for the scCO$_2$-saturated and highest for the brine-saturated sample. We also observe fewer AEs during pore-pressure reactivation of the fracture than during axial reloading (stress increase). Overall, the difference between fracture reactivation criteria for each test remains small, and we do not expect significant weakening of this deep reservoir sandstone analogue due to CO$_2$ injection. Additional tests using different materials are recommended to form a more robust conclusion on the influence of fluid saturation on fracture reactivation criteria. In such future tests, other factors such as the orientation and geometry of fractures should be thoroughly considered.

The scCO$_2$-saturated sample produces the greatest number of high magnitude AE events, and the brine-scCO$_2$ mixture generates the highest number of low magnitude events (Fig. 4), which may suggest event magnitude can be used as a fluid-type indicator in the shearing phase. Note that Griffiths et al. (2021) shows the results for all four test stages of shearing, sliding, pore pressure reactivation and axial loading reactivation. The brine-saturated sample gives the lowest number of AE events in total (Table 4). These results are in line with the hydraulic fracturing test by Ishida et al. (2016), where more events are detected for samples containing super-critical and liquid CO$_2$ than for samples containing viscous water or oil. The simulation results in the next section (Fig. 12) also lead to a similar conclusion. The higher mobility of CO$_2$ allows to travel faster and further into the host rock matrix, which we anticipate may generate more widely-spread and smaller-size fractures. We note that the relationship between the number of events and fluid type may also be linked to AE attenuation due to patchy saturation and squirt flow (Dautriat et al., 2016). In presence of brine, these effects may shift the frequency content of the AE or decrease the signal amplitude to below the detection threshold. Another potential cause of the high number of low magnitude events where both scCO$_2$ and brine are present could be due to salt-precipitation within the pore space, resulting in additional, low energy AE due to the crushing of NaCl crystals during compression (Rathnaweera et al., 2014).

Fig. 5 shows that the dominant frequency of first arrivals of AE events is also sensitive to fluid type during fracture reactivation by axial reloading. Namely, the dominant frequency is lower for the scCO$_2$- and scCO$_2$-brine-saturated sample than for the brine-saturated sample. This observation could be potentially linked to fluid viscosity (Benson et al., 2014; Clarke et al., 2019) or squirt flow effects, as mentioned previously

(Dautriat et al., 2016). Inferred AE source mechanisms are similar between tests and are generally characterized as compressive, with varying amounts of shear depending on test phase (Griffiths et al., 2021). We may conclude for the reactivation phases that there is little difference between fracture source mechanisms due to the stress path to reactivation or the presence of different fluids.

3.2. Material models and microseismicity potential of North Sea lithologies

Here, we briefly summarize the extensive rock mechanical testing (including multistage triaxial tests) performed on the Troll/Sognefjord sandstone, Visund sandstone, Draupne shale and Nordland mudstone. The tests are performed to determine the elastic and failure properties of the reservoir sandstones, and the shale/mudstone cap rocks. The tests include fracturing through triaxial testing and fracture re-activation, always accompanied by AE acquisition. At the end, we also provide the feasibility and implication of MS monitoring for CO$_2$ injection within potential storage sites in the North Sea based on AE data and interpretation. More detail may be found in CLIMIT, 2020 and Grande et al. (2020).

The effective vertical and horizontal consolidation stresses for the test representing Smeaheia site are chosen to be 13.3 MPa and 5.4 MPa, respectively, close to *in-situ* stress at injection point 1488 m TVD msl prior to depletion from nearby Troll field. The shear stress for fracture reactivation is calculated assuming a 45° fracture angle. Two tests (T2320 and 3041, Table 1) are performed using oil and a brine-scCO2 mixture, respectively, as pore fluid. Failure criteria are similar for both pore fluids. A linear regression is given for each of the fracture reactivations: The friction angle for each test is calculated from the arctangent of the slope of the linear regression; the apparent cohesion is the intercept with the y- (shear-stress) axis. The remobilization of the induced fracture results in a friction angle of 30° and an apparent cohesion of 0.8 MPa for T2320 (Fig. 6a). For the sample saturated in brine and scCO$_2$ (Test 3041), the effective axial stress is 25.6 MPa at failure. The fracture reactivation stages produce a slightly lower friction angle of 27° and an apparent cohesion of 1.76 MPa (Fig. 6a). However, if we assume the fractures are cohesionless, we obtain similar friction angles of 33.8° (Marcol 52, T2320) and 34.6° (brine+scCO$_2$, 3041). This suggests that the pore fluid type may have little effect on the fracture mechanical properties. These failure criteria may be studied alongside geomechanical modeling of the reservoir and overburden to assess the risk of fault reactivation and the potential for microseismicity. A low number of AE events are observed for the stress path relevant for CO$_2$ injection, indicating little microstructural damage to the Troll sandstone.
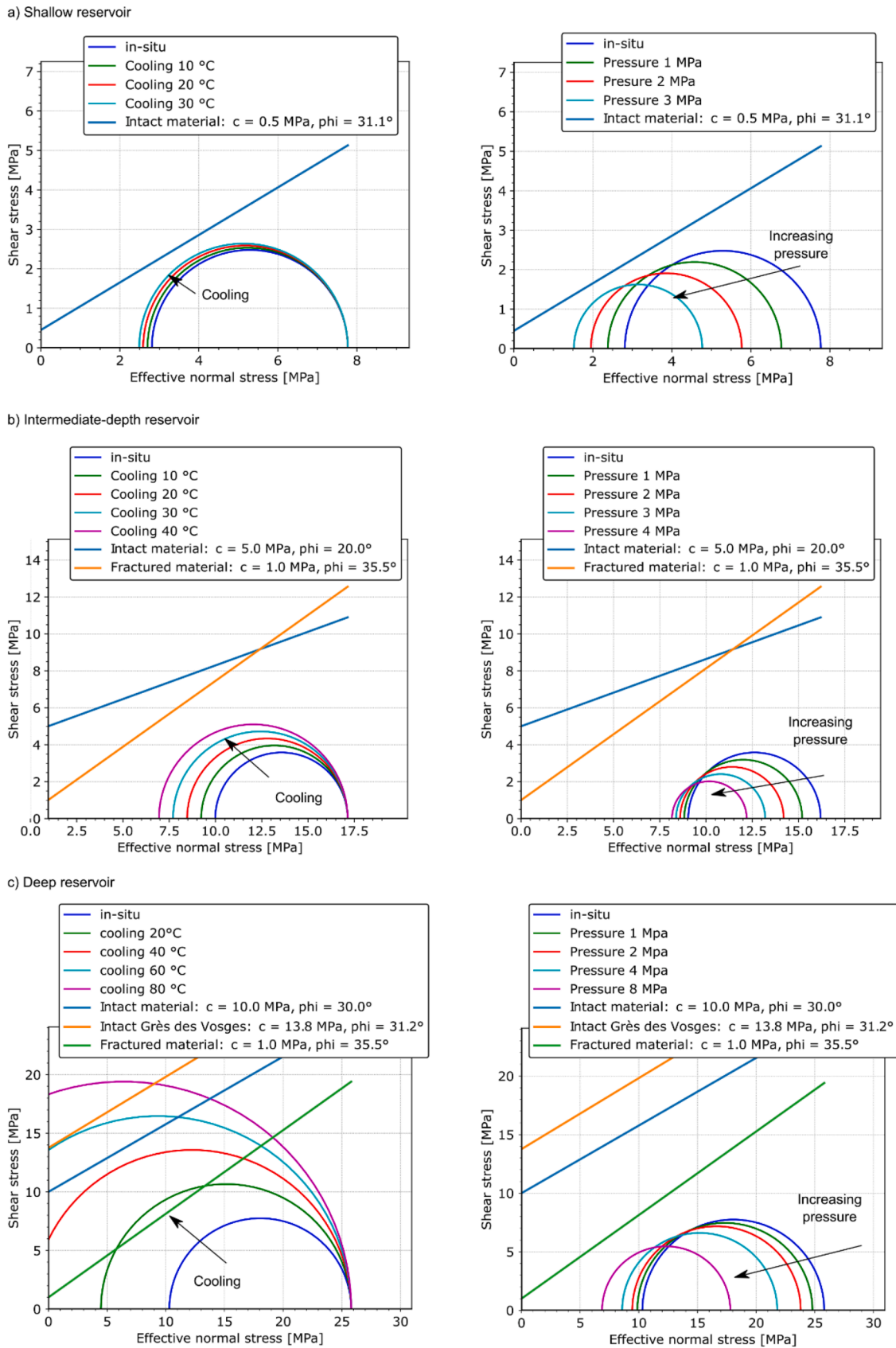
Fig. 3. Stress path in reservoir sandstone at three depths of shallow, intermediate and deep (top to bottom): thermal influence zone with effect of temperature alone (left column); and far field zone with effect of pore pressure alone (right column). Note that in the intermediate-depth plots (middle), the failure line of fractured material tested herein has much higher friction angle than that of intact rock, although the opposite would have been intuitively expected for same material. The two values are taken from different depths as well as different testing methods i.e. multistage for fractured rock vs. three single stage tests for intact rock.

Table 4

Summary for AE testing of Grès des Vosges sandstone: the number of AEs during each of the three phases of each test. Peak total axial stress and reactivation stresses (at 27 MPa total confining pressure and 9 MPa pore pressure), and Young's modulus (E$_{50}$). (CLIMIT, 2020; Griffiths et al., 2021).

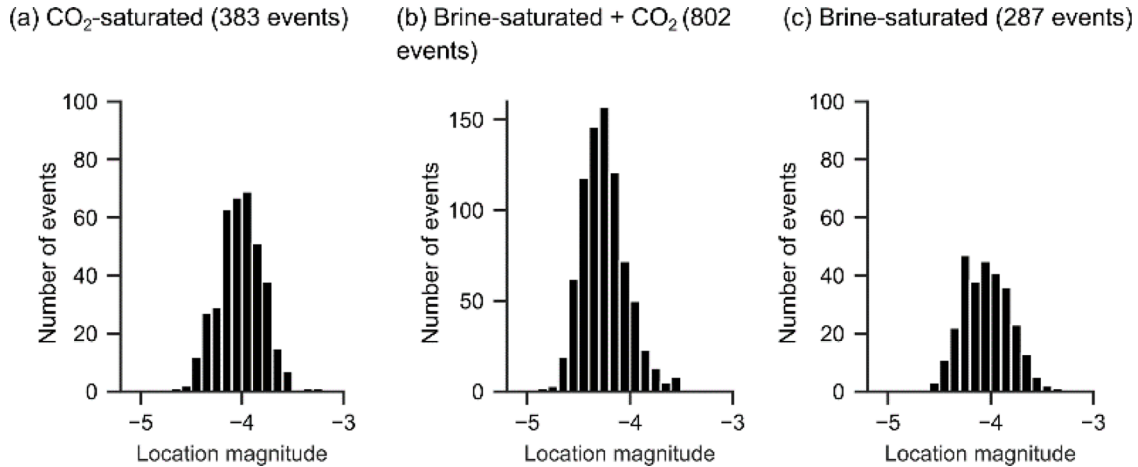| Test number (CSIRO) | Pore fluid | Number of AE during | | Pore pressure reactivation | Loading reactivation | Peak total axial stress [MPa] | E$_{50}$ [GPa] | Pp reactivation stress [MPa] | Loading reactivation stress [MPa] |
		Shearing	Sliding						
2862	CO$_2$	383	121	46	328	111.4	14.0	25.2	76
3037	brine-CO$_2$	802	397	19	93	107.2	12.0	25.8	79
3036	Brine	287	87	5	84	105.6	12.1	25.9	85

Fig. 4. Histograms of the magnitudes of located AE events during shearing phase. Note that the results for all the four phases are reported at CLIMIT, 2020 and Griffiths et al. (2021).
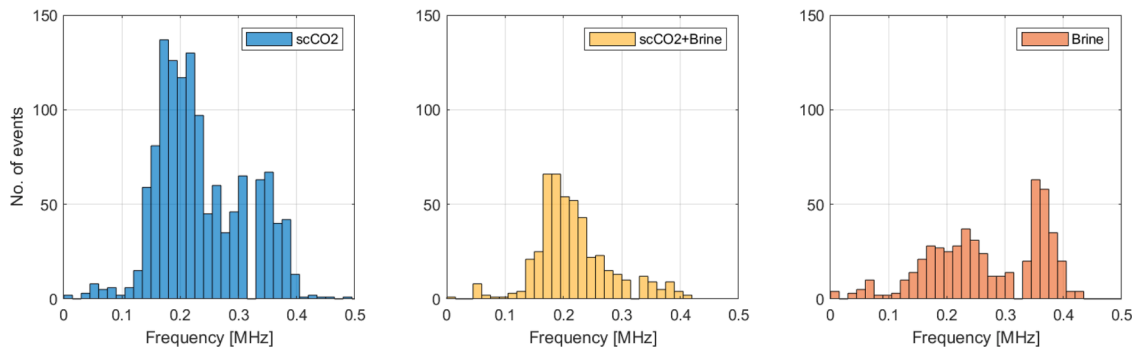

Fig. 5. Histogram to show dominant frequencies of P-wave first arrival waveforms calculated for axial reloading phase. Note that the results for all four phases are reported at CLIMIT, 2020 and Griffiths et al. (2021).

Three Visund samples are tested. The three samples are first confined at an isotropic pressure of 1 MPa before being placed under vacuum and then saturated with brine (35 g/L NaCl). At a rate of 3 MPa/hr, two of the three samples (T2409 and T2412) are then consolidated to 4 MPa cell pressure and 1 MPa pore pressure (3 MPa effective isotropic stress); the third sample (T2411) is consolidated to 2 MPa cell pressure and 1 MPa pore pressure (1 MPa effective isotropic stress). For T2409 and T2411, the samples are loaded axially from the effective isotropic stressess of 1 and 3 MPa, respectively, at a constant strain rate of 3 mm/m/hr (strain rate of 8.33×10^{-7}/s) until failure. For T2412, the axial stress is first increased from 3 MPa to 8 MPa effective axial stress, and then the pore pressure is increased at a constant rate of 0.5 MPa/hr until failure. In the latter case of T2412, the stress path approaching failure is a reduction in the effective mean stress at a constant shear stress. From the shear and normal stresses at failure (assuming a 45° fracture plane) for the three sample tests (T2409, T2411, and T2412), we determine a failure line, as shown in (Fig. 6b). Many AE events are recorded during

all the stress paths and are related to grain rotation, sliding, and breakage from compaction-dilation. However, no distinct failure plane is observed.

Two triaxial tests with the Draupne shale and Nordland mudstone are performed, resulting in clearly-defined through-going fractures and both of the cap rock samples dilated significantly during shearing (CLIMIT, 2020; Grande et al., 2020). The shear stress for fracture reactivation is calculated considering the macroscopic fracture angle (Fjær et al., 2008), as determined from a CT scan of the sample following the test (CLIMIT, 2020). We observe a more abrupt post-peak stress drop in the Draupne sample than the Nordland sample. From the fracture re-mobilization phase, the shear strength at the three different confining stresses gives friction angles and cohesions of 20.4° and 0.18 MPa for the Nordland sample, and 19.2° and 1.45 MPa for the Draupne sample (Fig. 7). For both the Nordland and Draupne lithologies, no AE event is recorded during the whole test period. The cap rocks are therefore believed to be aseismic during the effective stress unloading from the
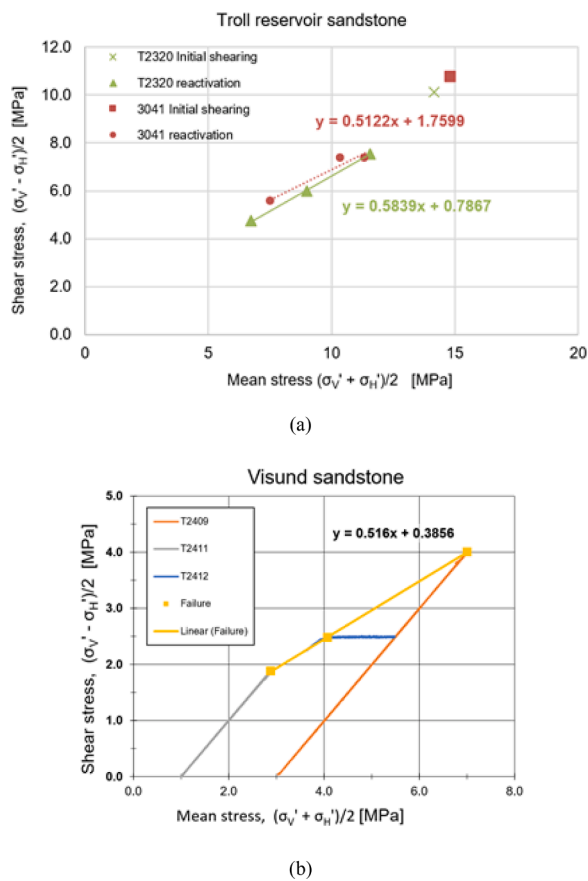
(a)

(a)

(b)

Fig. 6. (a) Failure criteria for Troll sandstone in shear stress vs. mean stress. (b) Failure criteria for Visund sandstone in shear stress vs. mean stress.

(b)

Fig. 7. (a) Failure criteria for Draupne shale in shear stress vs. mean stress.; (b) Failure criteria for Nordland mudstone in shear stress vs. mean stress.

in-situ stress, and the remobilization of the fracture at low confining stresses, which are the most representative test phases of a CO_2 injection scenario. Previous laboratory studies have detected AE from shale during deformation (Amann et al., 2011; Jia et al., 2018; Sarout et al., 2017), whose tests are yet mostly performed under uniaxial stress conditions (no confinement), or on partially-saturated samples. Combined with such research results in literature, our results suggest that at the small-scale and at the strain rates considered in the current study, cap rock may fail in a brittle but aseismic manner (including slow events, small-magnitude/untriggered signal, etc.), yet creating a distinct fracture (CLIMIT, 2020; Grande et al., 2020). Further investigation is required to assess this apparent aseismicity, potentially using lower frequency acoustic sensors or continuously-recorded AE as opposed to our current trigger-based data acquisition.

4. Advanced numerical simulation study

Advanced finite-element (FE) simulation approaches are developed and/or applied to better understand multiphase-flow and geomechanical behavior in relation to cold $scCO_2$ injection into the subsurface. Our goal is to answer the three following scientific questions:

- How different or similar is the geomechanical impact of the injection of $scCO_2$ into sandstone reservoir sealed by shale cap rock compared to brine injection?
- If the temperature of the injected $scCO_2$ is lower than that of the in-situ formations, what is the significance of thermal loading on the stress and strain field in the subsurface, and how can we quantify this effect?
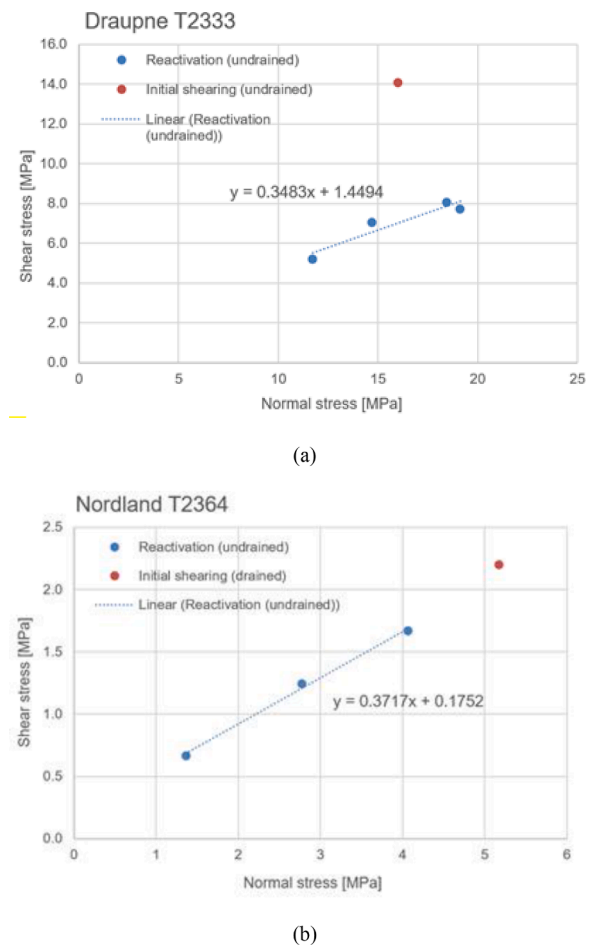- Should we expect any micro-seismicity at any of the storage sites in the North Sea e.g. in Smeaheia?

The 2D and 3D numerical models presented herein are set up on the basis of the Smeaheia model which is one of the representative geological models presented in the previous section. We use the numerical modeling simulators COMSOL Multiphysics, ABAQUS, and Code_Bright (Olivella et al., 1996). Fig. 8. shows the modeling workflow applied for 3D geomechanics modeling. The numerical modeling tools and workflow developed in IGCCS produce reasonable results which generally agree well with our expectations about the dominant physical processes governing the response of the system and the published literature. More importantly, all the simulation work done in IGCCS provides a better understanding of the coupled physical processes controlling the geomechanical behavior during CO_2 injection. A brief summary of the numerical simulation work done in IGCCS is provided here, and more details can be found in CLIMIT, 2020 and Bjørnarå et al. (2021a, 2021b).

4.1. 2D axis-symmetric reservoir modeling

We first simulate 2D axis-symmetric reservoir models and compare the $scCO_2$ and brine injection simulations to understand differences in the response of the system due to the coupled thermo-hydro-mechanical (THM) behavior. We consider two different injection rates of 5 Mt/yr and 1.3 Mt/yr (considered injection rates for the CO_2 storage prospect in Smeaheia) and a homogeneous initial thermal structure (COMSOL simulations). Supercritical CO_2 is injected at a temperature of about 15 °C below the reservoir's temperature. For the low injection rate, we also consider the case in which the initial thermal gradient is provided by the regional thermal gradient (Code_Bright simulations). Note that
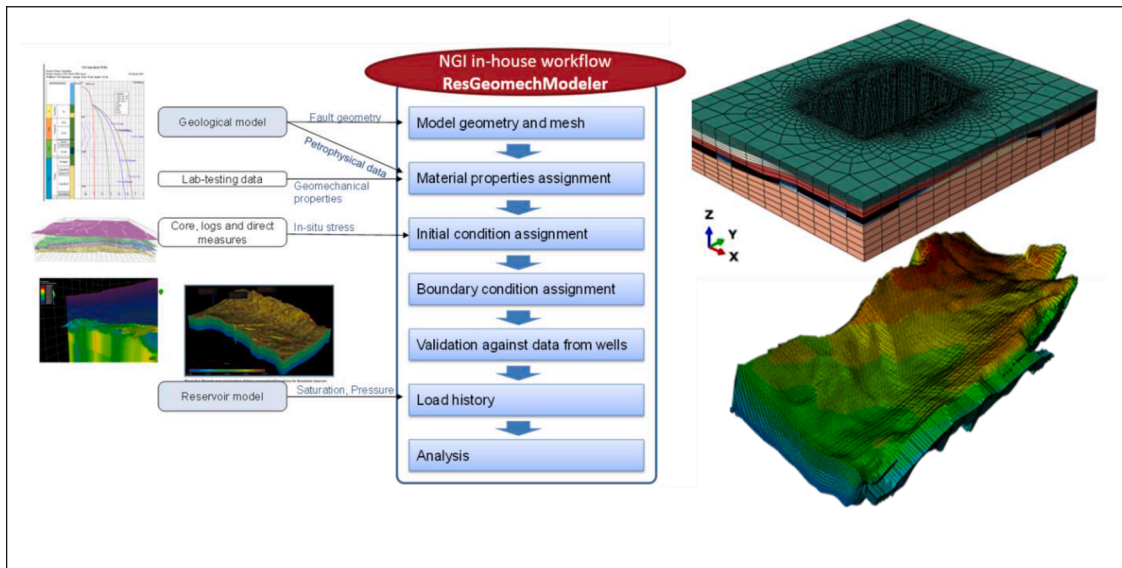
Fig. 8. (Left) Simulation workflow to build 3D geomechanics models by linking Eclipse, geomodel and Abaqus; (Right) FE model for the Smeaheia storage site (9 formation layers; 1.5 million grids; 8-node trilinear displacement and pore-pressure element (C3D8RP)).

the effect of overconsolidation on the thermal stress is known to be important (Favero et al., 2016) but not considered in the current study, mainly because the relevant information (related to uplift and/or erosion) is not fully quantified at the time of the simulation study. Fig. 9. shows the results for the high injection rate case in terms of changes in pore pressure, volumetric strain and water density at two selected locations: middle of the injection formation (Sognefjord, blue point), and 10 m above the reservoir/caprock interface (Draupne, red point). The pore pressure changes in the reservoir are relatively low, generally less than 1 MPa, and similar between both the HM- and THM models (the thin and thick blue lines coincide). However, the pore pressure changes in the caprock show clear differences between the two models. Namely, the HM-model shows a small pore pressure increase, as pressure increase in the reservoir slowly dissipates into the caprock (in the order of 1 bar, thin red line). In contrast, the THM model produces significant reduction in pore pressure in the caprock, by ca −3 MPa after about 10 years (thick red line). This different behavior between the HM and THM simulations because of cooling is also clearly observed in the volumetric strains. In the HM model (thin lines) the reservoir and caprock both show swelling due to reduced effective stress, while in the THM model (thick lines) they show contraction due to decreased total stress.

Fig. 10 shows the simulation results for the low injection rate (here 1.3 Mt/yr), where both the HM and THM models consider an initial temperature structure, before CO_2 injection, provided by a thermal

gradient of 35 °C/km (Gassnova, 2020). The results are presented for three different depths within the reservoir at the bottom, top and 100 m above the injection interval and at 0.25 m radial distance from injection. As also shown in Fig. 9, the pore pressure difference between the HM and THM models within the reservoir is negligible. The decrease in effective stress due to cooling is larger than that due to pore pressure increase. However, because of the initial thermal structure, thermal loading is not constant and depends on the vertical distance from injection. As expected, the decrease in effective stress due to cooling is larger closer to the injection area where the difference between the injected CO_2 temperature and the temperature of the background sediment is larger (Fig. 10, black dashed lines). The upward migration of CO_2 reduces the effect of thermal loading as the temperature of the injected CO_2 and the temperature of the background sediment becomes similar (Fig. 10, black dashed lines). In terms of volumetric strains, the THM simulation shows that thermal cooling can generate volumetric compression of the reservoir opposite to what we may expect by considering the HM simulation only. As discussed above, this change in volumetric strain behaviour due to thermal cooling disappears when the temperature of the injected CO_2 is similar to that of the surrounding sediment.
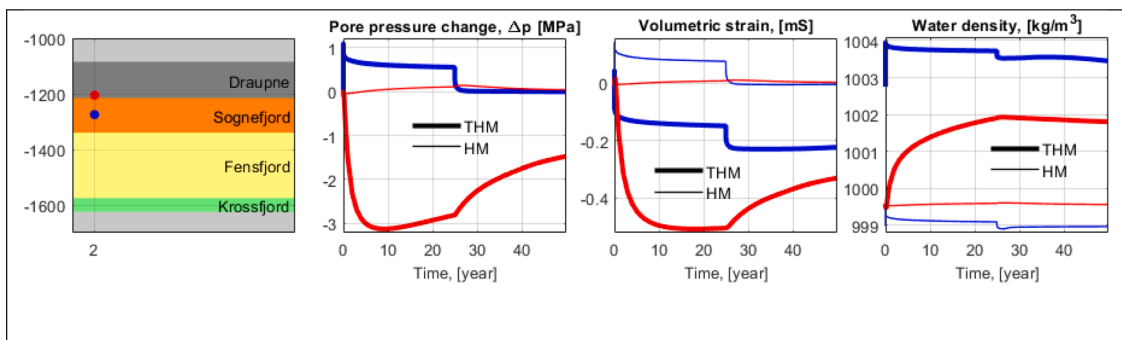

Fig. 9. Details of the change in pore pressure, volumetric strain (positive values mean expansion and negative compression), and water density in two selected locations 2 m laterally away from the symmetry axis: middle of the injection formation (Sognefjord, blue point), and 10 m above the reservoir/caprock interface (Draupne, red point). Thick lines are the solution from the THM-model, and the thin lines are from the HM-model. Note that for the pore pressure, the two blue lines almost coincide. The solution is for the high injection rate of CO_2 = 5 Mt/yr.
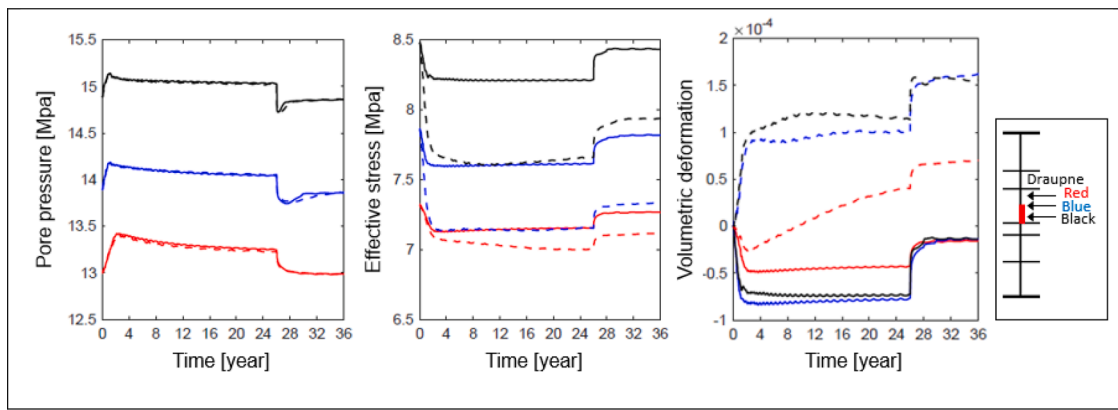
Fig. 10. Details of the change in pore pressure, effective stress and volumetric strain (negative values mean expansion and positive compression) in three selected locations within the reservoir for the low injection rate of 1.3 Mt/yr and at 0.25 m radial distance from the injection point. Here we consider the *in-situ* temperature structure of the system. Solid lines are results from HM simulations and dashed lines from THM simulations. In the inset, the thick red line indicates the injection interval.

4.2. 3D reservoir geomechanics modeling

By applying the 3D geomechanics modeling workflow shown in Fig. 8 (Left), the low injection rate scenario of 1.3 Mt/yr is simulated on the basis of the Smeaheia regional model shown in Fig. 8 (Right). Fig. 11 shows the results in terms of the stress states in the reservoir and caprock. Our results show that the low-rate injection scenario planned at the Smeaheia storage site is a safe operation as of today, and no induced-seismicity should be expected during the whole injection period of 25 years (Fig. 11; Choi et al., 2019), which also agrees well with the observations from the laboratory tests. However, if the injection rate is increased (e.g., up to 3–5 Mt/yr) and/or when more detailed information of the Smeaheia site is available (e.g., detailed description of the regional and reservoir-scale faults), these simulations should be re-done with the updated pressure and saturation dynamics.

4.3. Fracture propagation modeling

The numerical simulation of fracture generation and propagation caused by multiphase-flow is addressed by applying the so-called Cohesion Zone Modeling (CZM) approach, the detail of which can be found in Bjørnarå et al. (2021b). The main motivation is to investigate what differences should be expected between brine and CO_2 injection into a predefined weakness, e.g. fracture or fault, in the numerical simulation (Fig. 12). Note in Fig. 12 that the injection point is at (0,0) in the surface plot and the predefined fracture is specified along the *x*-axis ($y = 0$). In addition, two symmetric planes are imposed along the both the *x*- and *y*-axes, meaning that we solve only a quarter of the whole

domain. The results are shown in terms of pressure distribution Fig. 12. shows that the brine injection creates larger pressure perturbation than the CO_2 injection along the predefined fracture (> 20 m vs. ca 5 m, larger fracture by brine than CO_2 injection for a same injection time). In addition, brine injection shows the largest pressure gradient in front of the advancing fracture, while CO_2 injection shows the largest, albeit modest, pressure gradient laterally to the advancing front, which also results in a slower rupture velocity, producing lower frequency content in the micro-seismic signal. These observations related to fracture size and generation time agree well with the laboratory observations by Ishida et al. (2012) as well as in Fig. 5. Therefore, we believe that the CZM approach has good potential to improve our understanding of the key mechanisms controlling fracture and fault (re)activation. It should also be noted that all the parameters input to the CZM modeling should be quantified e.g. based on laboratory tests in order to produce good history matching results when compared with real data.

5. Field-scale analysis with focus on slow events

Slow earthquakes (i.e. slow-slip, low-frequency events or LFE, very-low-frequency events or VLF, non-volcanic tremor) are a family of identified, yet not fully understood, seismic events at tectonic scales (Ide et al., 2007a). Nevertheless, their potential link to high-pressure fluid migration reducing effective stress along fault planes (Obara, 2002; Ide et al., 2007b) makes them relevant to be investigated in the setting of industrial operations such as CO_2 storage. As of today, the closest analogues to slow earthquakes identified within industrial fluid injections are long-period-long-duration events (Das and Zoback, 2013).
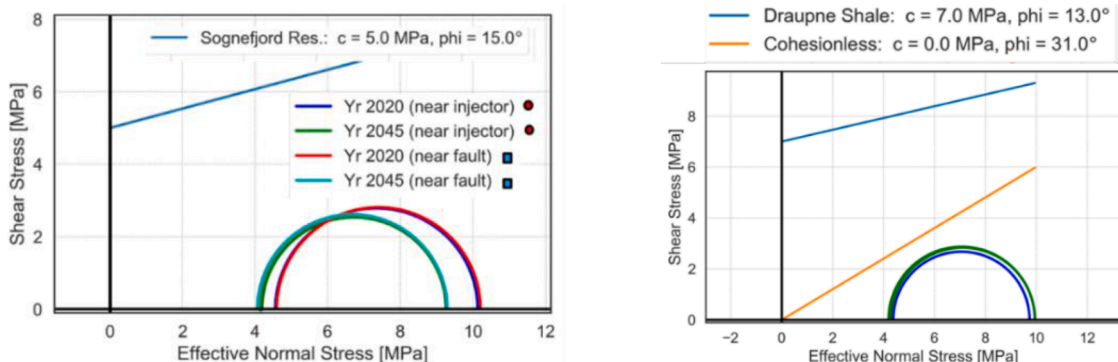

Fig. 11. Stress state in reservoir induced by the 1.3 Mt/yr injection rate for 25 years. The cohesions and friction angles used in plot are taken from Gassnova (2020) and differ slightly from values used in Table 2 and Fig. 3 in this paper.
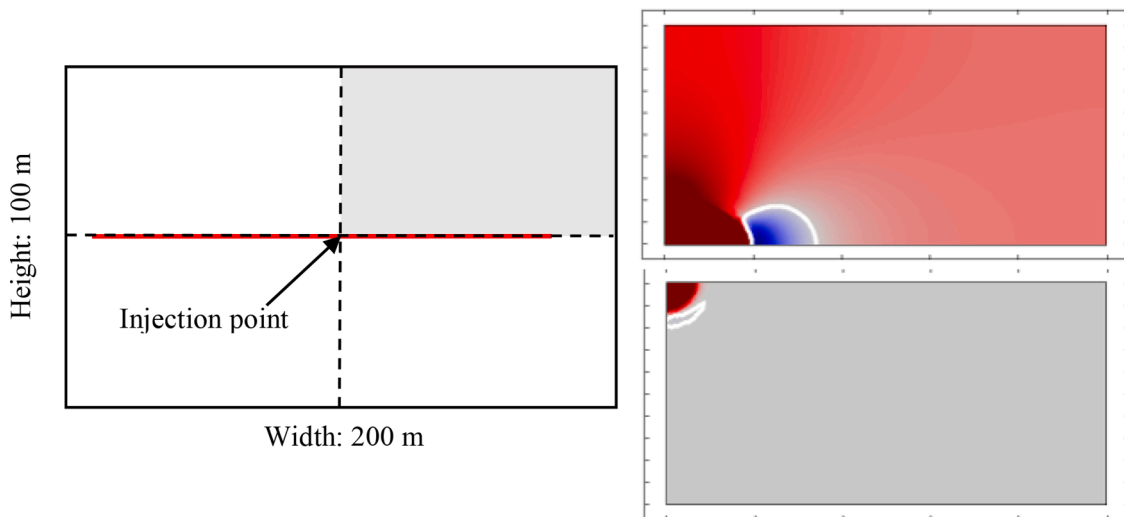
Fig. 12. (Left) Geometry of CZM-model: Red line is the pre-existing weakness; injection point is in the middle of the weakness; the simulated domain is the grey-shaded area (100 m). (Right) Pore pressure change distribution at a given time (here 200 s) during injection-induced fracture propagation: (Right upper) water injection into water; (Right lower) CO_2 injection into CO_2. Note that the white contour indicates zero pore pressure change, and the color-scale is symmetric where (cold) blue color represents negative relative pressure change and (hot) red represents positive relative pressure.

However, reasonable doubt on their origin has been cast as they have also been linked to regular, regional earthquake signals (Caffagni et al., 2015; Zecevic et al., 2016; Chen et al., 2018). In IGCCS, we investigated this topic via a synthetic data study. Numerical modeling of tremor-like signals requires several parameters, some of which have to date no observational reference at industrial fluid-injection scales. Hence, we modeled tremor-like signals constraining the modeling parameters based on observations from previous fluid-injection examples and tectonic studies (Table 5). This first-order approximation should be enough to produce signals with characteristics that resemble non-volcanic tremors at tectonic scales but with time and frequency characteristics that could be expected at scales of CO_2 injections.

VLF signals have been reproduced via band-pass filtering of shorter duration LFE signals, which in turn have been interpreted as arising from the fast activation of patches contained within a slowly slipping larger structure (Gomberg et al., 2016). Thus, while the larger structure can be considered in slow-slip aseismic activation, the tremor observed as spatially and temporally clustered LFEs would be the result of rapid slip along localized asperities. We followed this conceptual model to simulate tremor signals produced by the activation of patches distributed over a finite fault stimulated by CO_2 injection at field-scale.

Fig. 13 summarizes one of the examples studied. It considers a vertical fault plane striking in the north direction and located at depths between 2.375 and 2.625 km (see Table 5 for additional modeling details). Observed on the records of one sensor (Fig. 13b), the tremor-like displacement synthetics look like transient increases of the background noise. It is only when records from arrays of more closely spaced sensors are displayed together that coherent regions of constructive and destructive interference become obvious, clearly uncovering the presence of the tremor-like signal (Fig. 13c). Still, considering that the origin of tremor events is most likely within patches of larger faults, it is possible that their corresponding lower-magnitude signatures could be more often hidden below the background noise level of fluid-injection seismic monitoring records (Fig. 13d). Furthermore, their characteristic lower frequency compared to the seismic events they are generally associated with, suggests that sensors with lower frequency sensitivity than the geophones normally employed in industrial applications might be necessary for better signal detection and characterization. As part of the modeling work, we also observed that a location method based on imaging over a grid of potential source locations could make evident the presence of the tremor sources. Fig. 13e presents imaging results for this

example in map and side views for five subsequent, 260 s windows of the data plotted in Fig. 13d. These results show clearly the presence of the finite source close to the depth of 3 km. Nevertheless, for different experiments the geometry of the monitoring network played a role on the uncertainty of the location results as with conventional imaging of microseismic sources.

During the laboratory experiments with $scCO_2$ and brine saturated sandstone samples (shown earlier), fewer AEs are detected during fracture reactivation phases via pore pressure increase compared to reactivation via axial loading. A possible explanation for this behavior is that an effective stress reduction by pore pressure increase along fracture planes first occurs, which might be then facilitating slow activation with accompanying tremor activity. As the detection system in the laboratory experiments is trigger-based, this activity would go undetected. Furthermore, the tests on cap rocks show no AEs recorded despite the through-going fractures created in the rock samples. As before, if tremor activity is generated during these experiments, its characteristics are supposed to be undetected with the triggered-based systems used in standard laboratory AE monitoring. These observations highlight that the challenges in detecting tremor signals are not limited to field-scale applications but are also present in controlled environments such as laboratory experiments. Our modeling experiment demonstrates that tremor-like signals could be migrated back to their origin even in Signal-Noise-Ratio scenarios below 1. Although under an ideal modeling setting, this is an encouraging result, which can be followed up in future work studying in more detail the requirements in terms of sensor distribution and instrument response characteristics necessary to detect this type of seismic activity at the field scale.

6. Summary and conclusion

Through a literature review and compiling data both publicly available and created in IGCCS, we first divide potential CO_2 storage sites in the North Sea into three groups depending on depth: shallow, intermediate, and deep. Each group has different geological histories and geomechanical characteristics, which are summarized in the study. The study shows that each group may show different geomechanical responses to CO_2 injection and that reservoir lithology plays an important role in terms of the MS response (for example, highlighting a potential aseismicity for the shale and mudstone). The combined effects of increasing rock stiffness and temperature contrast between the host rock

Table 5

Summary of parameters used for the modeling of slow microseismicity.

| Parameter	Value	Notes	Refs.
Hypocenter migration velocity	1 m/s	Chosen from a range of 0.1–10 m/s reported at tectonic scales.	Ide (2014)
Medium properties	$V_p = 2500$ m/s $V_s = 1450$ m/s $\rho = 2700$ kg/m3 Homogeneous	Values observed in sandstone analogues of North Sea reservoir rocks used in this work. The medium is homogeneous for simplicity.	
Fault dimensions and geometry	Vertical patch of 250×250 m divided in subsegments of 5×5 m and striking North (i.e., y-axis in our reference system)	Manually selected to represent a fault stimulated by CO_2 injection at field-scale.	
Magnitude distribution	Gutenberg-Richter b-value = 2 $-1.5 < Mw < -1$	The b-value and magnitude distribution reflect observations from tectonic tremor. The magnitude range was chosen to maintain consistency with the size of individual patch subsegments.	Hawthorne and Bartlow (2018)
Rupture-front propagation model	Unilateral rupture from south to north	Chosen for simplicity but could be based on patterns of tremor migration reported at tectonic scales.	
Source mechanism of subsegments	Drawn from normal distributions. The mean values equaled the geometry of the main fault with activation consistent with the unilateral rupture (i.e., strike slip). Standard deviations were 10°	This selection is meant to simulate each fault subsegment as an asperity with geometry and activation largely aligned with those of the main fault.	
Source model and corner frequency	Brune pulses with corner frequencies drawn from a normal distribution with mean of 10 Hz and standard deviation of 5 Hz.	Corner frequency selection is arbitrary but attempts to keep consistency with the dimensions of the fault subsegments and assuming lower corner frequencies than expected for standard seismicity. No reference values were found at tectonic scales.	Brune (1970)
monitoring network	different surface monitoring network configurations	several monitoring geometries were explored to investigate advantages and disadvantages for the detection of the simulated seismicity.	
modeling engine	ray tracing	finite differences were explored as well obtaining similar results. ray tracing was preferred owing to its lower computational cost.	
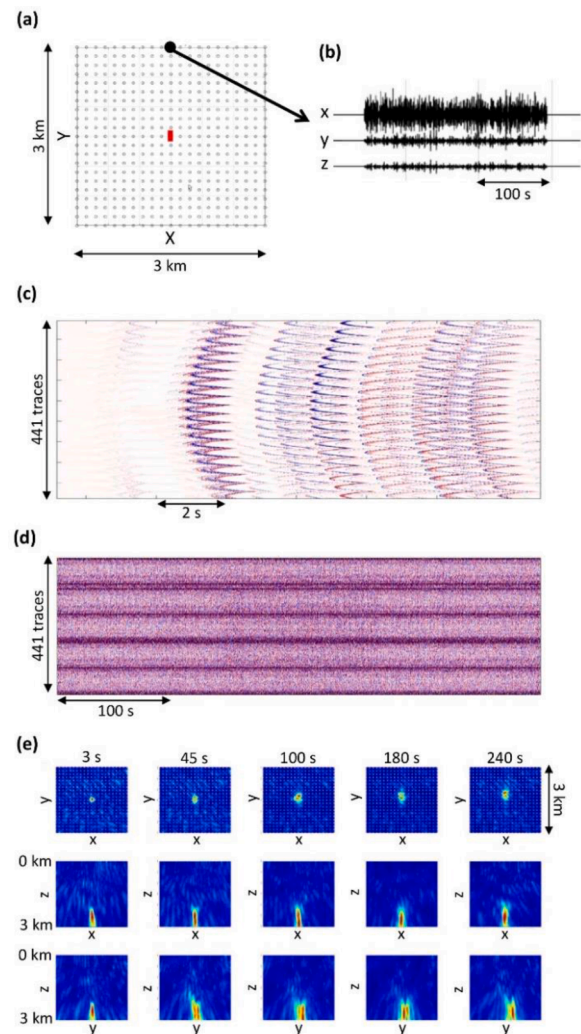
Fig. 13. (a) Map view showing an array of 441 surface receivers arranged in a rectangular grid with spacings of 150 m in both x and y directions. The red marker is the surface projection of the simulated fault (b) Example of simulated tremor synthetics for the three-components of one sensor (normalized per gather). (c) Zoom into the tremor synthetics for the vertical component of all the sensors in the array. (d) Tremor synthetics contaminated with industrial noise from a North Sea seismic installation. (e) Map and side views of imaging results at snapshots in time increasing from left to right. Synthetic amplitudes are normalized per trace in (c) and (d).

and injected CO_2 increase the failure risk of reservoir sandstones, potentially resulting in detectable micro-seismicity within the thermal influence zone. Thermal effects on the shale caprock are more complex and challenging to interpret due to its low permeability and undrained response at short timescales. Therefore, it is recommended that site-specific advanced THM-coupled numerical models should be deployed to accurately quantify such complex coupled phenomena, and is particularly critical for deep storage sites (e.g., Aurora).

The influence of pore fluid type and saturation on mechanical properties and MS response are investigated through a series of triaxial tests on sandstone samples containing brine, scCO_2, or a mixture of the two. Grès des Vosges sandstone is selected as an analogue to the Johansen Formation (targeted at the Aurora storage site). The scCO_2-saturated sample shows the highest strength and stiffness. The pore pressure required for fracture reactivation increases slightly with scCO_2 saturation, and the reactivation stress by axial reloading increases with brine saturation. The brine-scCO_2-saturated produced the greatest number of low magnitude AE events, and the scCO_2-saturated gives the

greatest number of high magnitude AE events. The AE response is more energetic and at higher frequency during fracture reactivation at higher effective stresses (by axial reloading) than at lower effective stresses (by pore pressure increase). In addition, the frequency spectrum of AE signals shows a fluid-type dependency of the dominant frequency, i.e. the lower dominant frequency is observed for the scCO_2-saturated as compared to the brine-saturated. How to apply all these learnings for field-scale MS monitoring is very relevant, and experience with field-scale data would be a key following-up.

Mechanical testing of natural North Sea lithologies provided information on their mechanical behavior under *in-situ* conditions and when subjected to effective stress changes due to CO_2 injection. In particular, the Troll Sognefjord Formation sandstone samples show inelastic deformation for the simulated temperature and stress changes due to injection (evidenced by AE). On the other hand, the Visund sandstone shows a very different mechanical behavior, with no apparent failure plane in the AE locations and the AE events occur at very low strains. These results suggest that a non-linear elasticity model for the Visund sandstone may be required for geomechanical modeling, even at small strains. In contrast, the Draupne and Nordland cap rocks are completely aseismic in the observed frequency range and under the tested stress conditions. Through advanced multistage triaxial testing with fracture reactivation, we determine frictional and cohesion properties of fractures in the Troll sandstone, Draupne shale and Nordland mudstone. The reactivation criteria for small fractures within these lithologies is essential to assess the risk of failure. For example, based on the determined reactivation criteria and the 3D geomechanical simulation, it is suggested that there is no high failure risk in the Smeaheia site with a 1.3 Mt/yr injection scenario.

The numerical simulation tools and workflow developed in IGCCS provide results that agree with our thermo-hydro-mechanical understanding of the system and the literature, as well as giving new relevant insights. The scCO_2 injection simulation shows very different behavior in terms of stress-strain changes compared to brine injection, particularly for the thermally-induced behavior. Furthermore, the numerical simulation approach for the multiphase-flow-driven fracture generation and propagation shows strong potential to improve our understanding of key mechanisms for fracture and fault activation during fluid injection. We have also investigated the slow-earthquake potential by synthesizing tremor-like signals based on previous fluid-injection examples and tectonic-scale observations. This first-order approximation produces characteristic signals that resemble non-volcanic tremors at tectonic scales but with time and frequency characteristics at the scale of CO_2 injection. When recording arrays are closely spaced, coherent regions of constructive and destructive interference become obvious. Still, it is possible that their corresponding lower-magnitude signatures could be hidden below the background noise level of fluid-injection seismic monitoring records. Their characteristic lower frequency suggests that sensors with lower frequency sensitivity than the geophones normally employed in industrial applications might be necessary for better signal detection and characterization.

The IGCCS project (which ran from May 2017 to October 2020) has filled some knowledge gaps that are relevant for MS monitoring and related geomechanical quantification of CO_2 storage candidate sites in the North Sea through advanced laboratory testing, THM-coupled numerical simulation, and field-scale seismic data processing and interpretation. It has delivered a new dataset of geomechanical properties of direct and analogue samples from the North Sea. This new dataset provides a solid and unique foundation for upcoming CCS-related research and commercial projects in the North Sea.

Declaration of Competing Interest

The authors declare that they have no known competing financial interests or personal relationships that could have appeared to influence the work reported in this paper.

References

Amann, F., Button, E.A., Evans, K.F., Gischig, V.S., Blümel, M., 2011. Experimental study of the brittle behavior of clay shale in rapid unconfined compression. Rock Mech. Rock Eng. 44, 415–430. https://doi.org/10.1007/s00603-011-0156-3.

Arts, R., Chadwick, A., Eiken, O., Thibeau, S., Nooner, S., 2008. Ten years' experience of monitoring CO_2 injection in the Utsira Sand at Sleipner offshore Norway. First Break 26, 65–72.

Benson, P.M., Vinciguerra, S., Nasseri, M.H.B., Young, R.P., 2014. Laboratory simulations of fluid/gas induced micro-earthquakes: application to volcano seismology. Front. Earth Sci. 2 https://doi.org/10.3389/feart.2014.00032.

Bjørnarå, T.I., Park, J., Marin-Moreno, H., 2021a. Geomechanical Integrity and Non-Isothermal Effect in CO_2 Storage. GHGH-15, Abu Dhabi, UAE.

Bjørnarå, T.I., Park, J., Jostad, H.P., 2021b. Hydraulic Fracturing: Micro-Seismicity and Fluid-Type Dependency. GHGH-15, Abu Dhabi, UAE.

Brune, J., 1970. Tectonic stress and the spectra of seismic shear waves from earthquakes. J. Geophys. Res. 75, 4997–5009.

Caffagni, E., Eaton, D., van der Baan, M., Jones, J., 2015. Regional seismicity: a potential pitfall for identification of long-period long-duration events. Geophysics 80, A1–A5.

Chen, H., Niu, F., Tang, Y., Tao, K., 2018. Toward the origin of long-period long-duration seismic events during hydraulic fracturing treatment: a case study in the shale play of Sichuan basin, China. Seismol. Res. Lett. 89, 1075–1083.

Choi, J.C., Skurtveit, E., Grande, L., Park, J., 2019. Effect of CO_2 injection-induced stress rotation in overburden on the fault stability and induced seismicity: numerical investigation. In: Proceedings of the Trondheim CCS Conference TCC10, 18th June 2019.

Clarke, J., Adam, L., Sarout, J., van Wijk, K., Kennedy, B., Dautriat, J., 2019. The relation between viscosity and acoustic emissions as a laboratory analogue for volcano seismicity. Geology 47, 499–503. https://doi.org/10.1130/G45446.1.

Das, I., Zoback, M., 2013. Long-period, long-duration seismic events during hydraulic stimulation of shale and tight-gas reservoirs – part 1: waveform characteristics. Geophysics 78, KS97–KS108.

Dautriat, J., Sarout, J., David, C., Bertauld, D., Macault, R., 2016. Remote monitoring of the mechanical instability induced by fluid substitution and water weakening in the laboratory. Phys. Earth Planet. Inter. 261, 69–87. https://doi.org/10.1016/j.pepi.2016.06.011.

Elenius, M., Skurtveit, E., Yarushina, V., Baig, I., Sundal, A., Wangen, M., Landschulze, K., Kaufmann, R., Choi, J.C., Hellevang, H., Podladchikov, Y., Aavatsmark, I., Gasda, S., 2018. Assessment of CO_2 storage capacity based on sparse data: skade Formation. Int. J. Greenh. Gas Control 79 (2018), 252–271.

CLIMIT, 2020. Induced-seismicity geomechanics for controlled CO2 storage in the North Sea (IGCCS), CLIMIT project final report KPN-268520/E20, https://www.researchgate.net/publication/354853587_Induced-seismicity_Geomechanics_for_Controlled_CO2_Storage_in_the_North_Sea.

Equinor (2020) Sharing data from Northern lights well https://www.equinor.com/en/news/20201019-sharing-data-northern-lights.html.

Favero, V., Ferrari, A., Laloui, L., 2016. Thermo-mechanical volume change behaviour of opalinus clay. Int. J. Rock Mech. Min. Sci. 90, 15–25.

Fawad, M., Mondol, N.H., 2019. Comparison of sealing properties of Amundsen and Drake formations for potential CO_2 storage in North Sea. In: Proceedings of the 81st EAGE Conference and Exhibition 2019. European Association of Geoscientists and Engineers (EAGE). ISBN 978-1-5108-9281-1.

Fjær, E., Holt, R.M., Raaen, A.M., Risnes, R., Horsrud, P., 2008. Petroleum related rock mechanics. ed Developments in Petroleum Science, 2 ed. Elsevier, Amsterdam.

Gassnova (2020), Smeaheia dataset: rockmechanical data for Smeaheia studies, https://co2datashare.org/dataset/smeaheia-dataset.

Gomberg, J., Agnew, D., Schwartz, Y., 2016. Alternative source models of very low frequency events. J. Geophys. Res. 121, 6722–6740.

Grande, L., Cuisiat, F., 2008. Predicting deformation properties of argillaceous sediments for geo-mechanical analysis. In: Proceedings of the 33 International Geological Conference. Lillestrøm, 8 August 2008.

Grande, L., Griffiths, L., Park, J., Choi, J.C., Bjørnarå, T.I., Sauvin, G., Mondol, N.H., 2020. Acoustic emission testing of shales for evaluation of microseismic monitoring of North Sea CO_2 storage sites. In: Proceedings of the 82nd EAGE Conference & Exhibition.

Griffiths, L., Dautriat, J., Vera Rodriguez, I., Iranpour, K., Sauvin, G., Park, J., Sarout, J., Soldal, M., Grande, L., Oye, V., Dewhurst, D.N., Haque Mondol, N., Choi, J.C., 2019. Inferring microseismic source mechanisms and *in situ* stresses during triaxial deformation of a North-Sea-analogue sandstone. Adv. Geosci. 49, 85–93. https://doi.org/10.5194/adgeo-49-85.

Griffiths, L., Dautriat, J., Park, J., Rodriguez, I.V., Iranpour, K., Sauvin, G., Sarout, J., Grande, G., Oye, V., Soldal, M., Dewhurst, D.N., Mondol, N.H., Choi, J.C., 2021. The Influence of Super-Critical CO_2 Saturation on the Mechanical and Failure Properties of a North Sea Reservoir Sandstone Analogue. GHGH-15, Abu Dhabi, UAE.

Hansen, J.A., Yenwongfai, H.D., Fawad, M., Mondol, N.H., 2017. Estimating exhumation using experimental compaction trends and rock physics relations, with continuation into analysis of source and reservoir rocks: central North Sea, offshore Norway SEG technical program expanded abstracts. Soc. Explor. Geophys. 2017 (2017), 3971–3975. https://doi.org/10.1190/segam2017-17783053.1.

Hawthorne, J., Bartlow, N., 2018. Observing and modeling the spectrum of a slow slip event. J. Geophys. Res. 123, 4243–4265.

Horsrud, P., 2001. Estimating mechanical properties of shale from empirical correlations, SPE drilling and completion, 16 02, 68–73.

Ide, S., 2014. Modeling fast and slow earthquakes at various scales. Proc. Jpn. Acad. Ser. B Phys. Biol. Sci. 90, 259–277.

Ide, S., Beroza, G., Shelly, D., Uchide, T., 2007a. A scaling law for slow earthquakes. Nature 447, 76–79.

Ide, S., Shelly, D., Beroza, G., 2007b. Mechanism of deep low frequency earthquakes: further evidence that deep non-volcanic tremor is generated by shear slip on the plate interface. Geophys. Res. Lett. 34, L03308.

Ishida, T., Aoyagi, K., Niwa, T., et al., 2012. Acoustic emission monitoring of hydraulic fracturing laboratory experiment with supercritical and liquid CO_2. Geophys. Res. Lett. 39 https://doi.org/10.1029/2012GL052788.

Ishida, T., Chen, Y., Bennour, Z., Yamashita, H., Inui, S., Nagaya, Y., Naoi, M., Chen, Q., Nakayama, Y., Nagano, Y., 2016. Features of CO 2 fracturing deduced from acoustic emission and microscopy in laboratory experiments. Journal of.

Jia, S.Q., Eaton, D.W., Wong, R.C., 2018. Stress inversion of shear-tensile focal mechanisms with application to hydraulic fracture monitoring. Geophys. J. Int. 215, 546–563. https://doi.org/10.1093/gji/ggy290.

Mondol, N.H., Grande, L., Aker, E., Berre, T., Ørbech, T., Duffaut, K., Jahren, J., Bjørlykke, K., 2010. Velocity anisotropy of a shallow mudstone core. In: Proceedings of the EAGE Shale Workshop 2010a, Shale – Source & Challenge, 26-28 April 2010.

Mondol, N.H., Fawad, M., Park, J., 2018. Petrophysical analysis and rock physics diagnostics of Sognefjord formation in the Smeaheia area, Northern North Sea. In: Proceedings of the 5th CO_2 Geological Storage Workshop. Utrecht, the Netherlands. https://doi.org/10.3997/2214-4609.201802951, 21-23 November.

Mondol, N.H., 2019. Geomechanical and seismic behaviors of Draupne shale: a case study from the central North Sea. EAGE extended abstract. In: Proceedings of the 81st EAGE Annual Meeting. London, UK. https://doi.org/10.3997/2214-4609.201800675, 3-6 June 2019.

Norwegian Petroleum Directorate. CO2 storage Atlas – Norwegian continental shelf. https://www.npd.no/en/facts/publications/co2-atlases/co2-atlas-for-the-norwegian-continental-shelf/.

Obara, K., 2002. Nonvolcanic deep tremor associated with subduction in southwest Japan. Science 296, 1679–1681.

Olivella, S., Gens, A., Carrera, J., Alonso, E., 1996. Numerical formulation for a simulator (CODE_BRIGHT) for the coupled analysis of saline media. Eng. Comput. 13 (7), 87–112 (Swansea).

Oye, V., Dando, B., Wuestefeld, A., Jerkins, A., Koehler, A., 2021. Cost-Effective Baseline Studies For Induced Seismicity Monitoring Related to CO_2 Storage Site Preparation. GHGH-15, Abu Dhabi, UAE.

Park, J., Vöge, M., Sauvin, G., 2017. 2.5D inversion and joint interpretation of CSEM data at Sleipner CO_2 storage. Energy Procedia 114, 3989–3996.

Rathnaweera, T.D., Ranjith, P.G., Perera, M.S.A., 2014. Salinity-dependent strength and stress–strain characteristics of reservoir rocks in deep saline aquifers: an experimental study. Fuel 122, 1–11. https://doi.org/10.1016/j.fuel.2013.11.033.

Sarout, J., Le Gonidec, Y., Ougier-Simonin, A., Schubnel, A., Guéguen, Y., Dewhurst, D. N., 2017. Laboratory micro-seismic signature of shear faulting and fault slip in shale. Phys. Earth Planet. Inter. 264, 47–62.

Skurtveit, E., Grande, L., Ogebule, O., Gabrielsen, R., Faleide, J., Mondol, N., Maurer, R., Horsrud, P., 2015. Mechanical testing and sealing capacity of the Upper Jurassic Draupne formation, North Sea. In: Proceedings 49th US Rock Mechanics/ Geomechanics Symposium. American Rock Mechanics Association.

Sundal, A., Miri, R., Ravn, T., Aagaard, P., 2015. Modelling CO_2 migration in aquifers considering 3D seismic property data and the effect of site-typical depositional heterogeneities. Int. J. Greenh. Gas Control 39, 349–365.

Sundal, A., Nystuen, J.P., Rørvik, K.L., Dypvik, H., Aagaard, P., 2016. The lower Jurassic Johansen formation, northern North Sea – depositional model and reservoir characterization for CO_2 storage. Mar. Pet. Geol. 77, 1376–1401.

Tveit, S., Mannseth, T., Park, J., et al., 2020. Combining CSEM or gravity inversion with seismic AVO inversion, with application to monitoring of large-scale CO_2 injection. Comput. Geosci. 24, 1201–1220. https://doi.org/10.1007/s10596-020-09934-9.

Zecevic, M., Guillaume, D., Jurick, D, 2016. On the nature of long-period long-duration seismic events detected during hydraulic fracturing. Geophysics 81, KS113–KS121.

Zhu, C., Zhanga, G., Lua, P., Meng, L., Ji, X., 2015. Benchmark modeling of the Sleipner CO_2 plume: calibration to seismic data for the uppermost layer and model sensitivity analysis. Int. J. Greenh. Gas Control 43 (2015), 233–246.